Transonic Euler Solutions on a Blunt, Body-Wing-Canard Configuration

Lawrence E. Lijewski*
U.S. Air Force Armament Laboratory, Eglin Air Force Base, Florida

The purpose of this investigation is to begin the validation process on a recently developed Euler code for multifinned bodies with low-aspect-ratio surfaces and to examine the aerodynamic effect of these fin surfaces on the configuration. Pressure distribution, local Mach number, and force and moment calculations are compared to wind-tunnel data for a cruciform, wing-canard body of revolution at angles of attack up to 12 deg. Near-sonic conditions at Mach 0.95 and 1.05 are predicted successfully and presented for body, wing, and canard surfaces. Effects of the wings and canards are examined by comparing body-wing-canard calculations with body-wing and body-alone predictions. An elliptic grid generator and explicit upwind Euler solver were used on a CRAY-XMP to obtain the results presented. The paper illustrates the inviscid code's capability to predict aerodynamic characteristics on geometrically complex configurations at near-sonic conditions and low-to-moderate angles of attack.

Nomenclature

B = body
BW = body-wing
BWC = body-wing-canard
C = canard root chord
C_M = pitching-moment coefficient
C_N = normal-force coefficient
C_P = pressure coefficient
C_P^* = sonic pressure coefficient
L = body length
M = freestream Mach number
M_L = local Mach number
W = wing root chord
X = axial Cartesian coordinate
XCP = center-of-pressure location/body length
α = angle of attack, deg
η = wing, canard span location/chord length
ϕ = body circumferential angle, deg

Introduction

ACCURATE prediction of free-flight aerodynamic characteristics of air vehicle shapes is of paramount importance to the airframe designer. Mission effectiveness is highly dependent on the designer's ability to design an airframe with desirable aerodynamic qualities to deliver the payload with optimum maneuvering performance. Often this is a time-consuming, iterative effort, coupling an aerodynamic predictive method and expensive wind-tunnel testing for airframe validation. In addition, the difficulty is compounded since modern tactical fighter aircraft operate primarily at transonic speeds. The desirable prediction method would be one that gives accurate free-flight aerodynamic characteristics for a geometrically complex airframe configuration. Just such computational techniques would enhance design procedures and reduce costly wind-tunnel validation testing. The focus of the current research and development in airframe design and aerodynamic predictions is to combine elliptic grid generation and Euler equation algorithms into a usable predictive air vehicle design tool. The effort began in 1983 with the derivation of a three-dimensional, arbitrary shape, elliptic grid generator and a split-flux vector-explicit Euler solver. The work presented here is an interim step in developing these techniques.

In computational aerodynamics, numerous efforts[1-7] have been directed at predicting transonic flows about body-wing configurations. The approaches have varied from potential to Navier-Stokes, but the majority of these efforts have been on either high-aspect-ratio transport aircraft wing configurations or at low transonic Mach numbers. Little has been done to compute near-sonic flows on air vehicle shapes with low-aspect-ratio wing and canard surfaces. Yet, it is precisely this type of configuration/flight regime combination that is of interest, since these vehicles are often deployed transonically. Recent work,[8] however, has demonstrated the feasibility of near-sonic computations on body-wing configurations suitable for preliminary design. This paper extends the previous work by adding low-aspect-ratio canards and making calculations at both Mach 0.95 and 1.05. The grid-generation and flow-solver approaches will be discussed briefly and results will be presented that investigate effects of Mach number and configuration complexity.

Configuration

The configuration selected was comprised of simple geometric curves to preserve a generic quality but with enough variation to produce a complex shock structure. Figure 1 illustrates the dimensions of the configuration. The body is composed of hemispherical, ogival, parabolic, cylindrical, and conic sections. The nose section has a bluntness ratio of 0.85 caliber. The wings, including the flap, comprise an airfoil section, flat plate, wedge, ogive, and tapered flat plate. The exposed aspect ratio is 0.848. The canards with an exposed aspect ratio of 0.617 are made up of a circular arc and a flat plate.

Approach

Grid Generation

To obtain an accurate flow solution, a smooth grid must be generated on which to solve the fluid flow equations. The algebraic/elliptic grid-generation method chosen was that by Thompson and Warsi,[9] Thompson,[10] and Martinez et al.[11] The

---

Presented as Paper 87-2273 at the AIAA 5th Applied Aerodynamics Conference, Monterey, CA, Aug. 17-19, 1987; received Jan. 7, 1988; revision received June 5, 1988.

*Senior Scientist, Computational Fluid Dynamics Section, Aerodynamics Branch, Aeromechanics Division. Senior Member AIAA.

grid-generation scheme uses boundary-conforming coordinate systems to treat boundaries of arbitrary shape. Control of the grid line spacing and orientation in the field is achieved by adopting a system of Poisson-like equations. For complex, three-dimensional configurations, it is often difficult to obtain a reasonable grid with the entire physical region transformed into single rectangular computational space. The preferred approach is to segment the physical region into contiguous subregions bounded by six curved surfaces, with each subregion transformed into a rectangular computational block. An individual grid is generated in each subregion and then patched together to form the overall grid. These patched blocks abut neighboring blocks with no overlap and with adjacent boundaries coincident in space. However, the first row of points inside each block act as a border of image points for the adjoining block in the solution of the grid-generation equations in the adjoining block. In this way, the blocks communicate with one another during each iteration and assure that the grid lines are continuous across block boundaries similar to that of Weatherill and Forsey.[5] For the wing-canard configuration, 12 subregion grids are generated. Three subregions or blocks are formed between each set of two wings and canards. A cross section of these three blocks is shown in Fig. 2. The outer and wing blocks are $75 \times 23 \times 13$ and the canard block is $53 \times 10 \times 13$. A frontal view, Fig. 3, looking downstream at the configuration further depicts the block system setup. Figure 3 is a cut through the outer and canard blocks at approximately $X/L = 0.13$, whereas Fig. 4 cuts through the wing block at $X/L = 0.67$. Clustering of the grid near the body and fins is clearly evident. When at angle of attack, the upper blocks—1, 5, and 9—are on the leeward side whereas the lower blocks—3, 7, and 11—are on the windward side. An overall view of the grid is illustrated in Fig. 5, showing a complete slice of the grid along with the back boundary plane. Figure 6 strips away much of the grid, leaving only a wireframe grid showing the block boundaries and the configuration location.

In comparing the effects of the wings and canards, additional grids were used for the body-wing and body-alone configurations. The body-wing grid was made of four blocks, with each block (140 x 24 x 10) running the entire length of the grid between two fins. Thus, the 360-deg grid was defined with four 90-deg blocks. The body-alone grid (96 x 15 x 10) was made of only one block wrapped 180 deg around the body, taking advantage of the plane of symmetry.

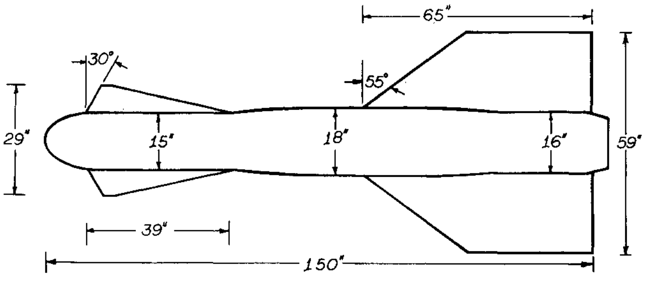

Fig. 1 Body-wing-canard configuration.

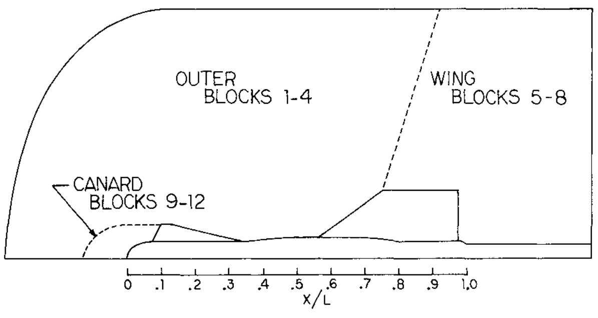

Fig. 2 Blocked grid system.

Euler Solver

The Euler equations have been transformed for use on a general curvilinear coordinate system. The three-dimensional Euler solver[12] is based on flux-vector splitting. The numerical scheme is an explicit, second-order, upwind scheme by Warming and Beam[13] stable for a Courant number of 2 or smaller. An advantage of the method is that it eliminates one variable by requiring no additional artificial dissipation. Although user control of artificial dissipation may be desirable in some cases, it is not necessarily preferred and it does add an additional variable to the process.

The Euler equations are written in strong conservation law form to capture discontinuities such as shocks in the flow. The scheme uses a finite-volume formulation to achieve total flexibility with regard to geometry. Local time stepping is used to accelerate convergence for steady-state problems. The code has been extended to a multiblock capability corresponding to the grid subregions discussed previously. This capability

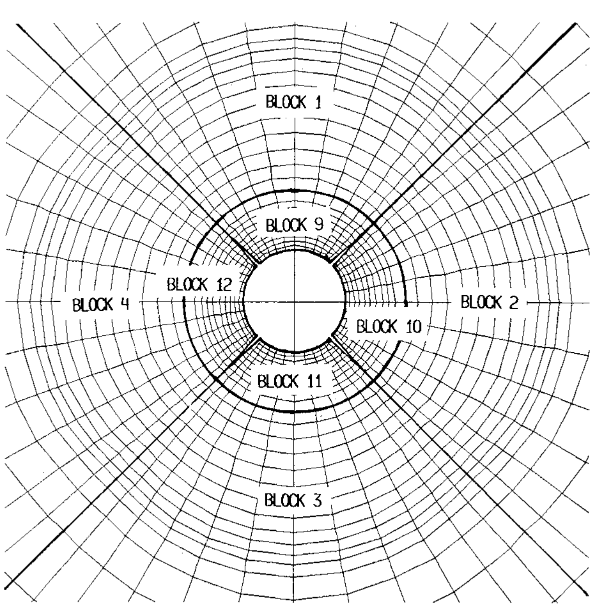

Fig. 3 Grid cross section at canard.

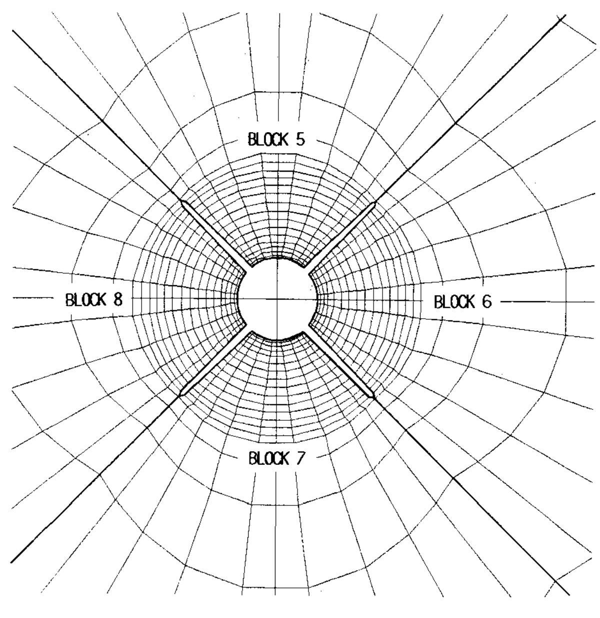

Fig. 4 Grid cross section at wing.

allows finned body flows to be calculated for angle-of-attack cases.

Consistent with the impetus leading to the split-flux form of the Euler equations, that is, honoring propagation directions of flow information, a set of boundary conditions, referred to as characteristic variable boundary conditions,[12] has been developed. Theoretically, the characteristic variable boundary conditions should model nature more accurately because of an ability to pass information into or out of the computational domain. Boundary conditions exist for both subsonic and supersonic inflow and outflow at outer boundaries and no-flow through impermeable wall conditions at body and fin surfaces. The interblock boundaries are purely notional boundaries with no physical significance. The fluid dynamic equations are solved second order at these boundaries by accessing two layers of cells in the adjacent block. Program logic automatically determines if these layers are used in the calculations. This depends on the sign of the eigenvalues locally in each boundary cell, which indicates the direction of propagation of flow information into or out of the block. Thus, the interblock boundary cells are treated as any other cells out in the grid field away from impermeable surfaces.

Computational Results

Using the Euler solver and multiblock grids, a series of computational cases is solved to determine the capabilities of the method. Results are obtained for Mach 0.95 and 1.05 at angles of attack up to 12 deg. All cases were run to convergence at 1000 iterations. The code typically performed at 4.6×10^{-5} s/point/iteration. For the body-wing-canard configuration, this translates into 2.65 h of run time on a CRAY-XMP using 3.6×10^6 words in-core and 14.1×10^6 words of solid-state device.

Configurational Effects

To examine the effects the wings and canards have on the configuration, cases were run at 9-deg angle of attack, Mach 0.95 and 1.05, for the following three combinations: body-alone, body-wing, and body-wing-canard. Figure 7 compares the pressure distributions on the leeward side of the body. Very good agreement between data and calculation is observed. The presence of the canard has a marked effect on the pressures in the nose region. Although reducing only slightly the initial expansion on the nose, compared to the body-wing case, the canard causes a re-expansion at $X/L = 0.15$, delaying the subsequent shock by 5% of the body length. This second expansion on the body coincides with a strong expansion on the canard airfoil section, which will be presented later. The canard continues to affect the flow downstream at the wing section. The expansion peak at $X/L = 0.78$ is stronger for the body-wing case, indicating that the canards create a downwash effect that lessens the angle of attack at the wings.

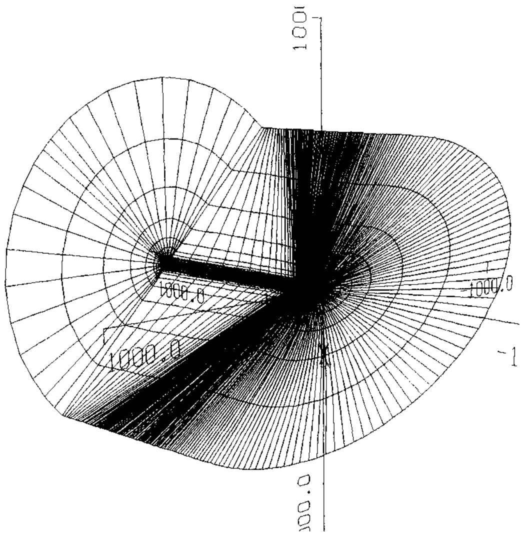

Fig. 5 Overall 12-block grid.

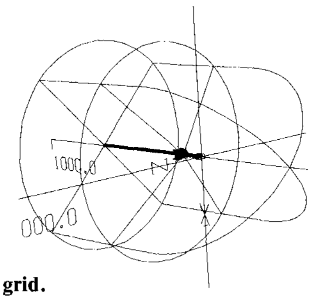

Fig. 6 Wireframe 12-block grid.

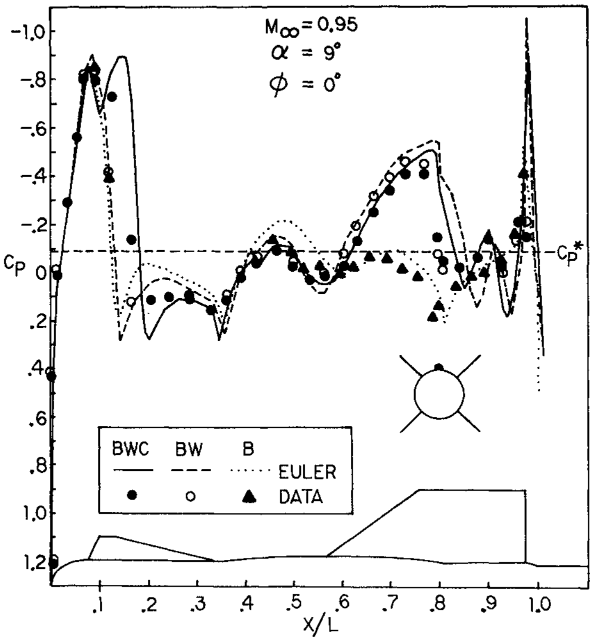

Fig. 7 Configurational effects, body leeside.

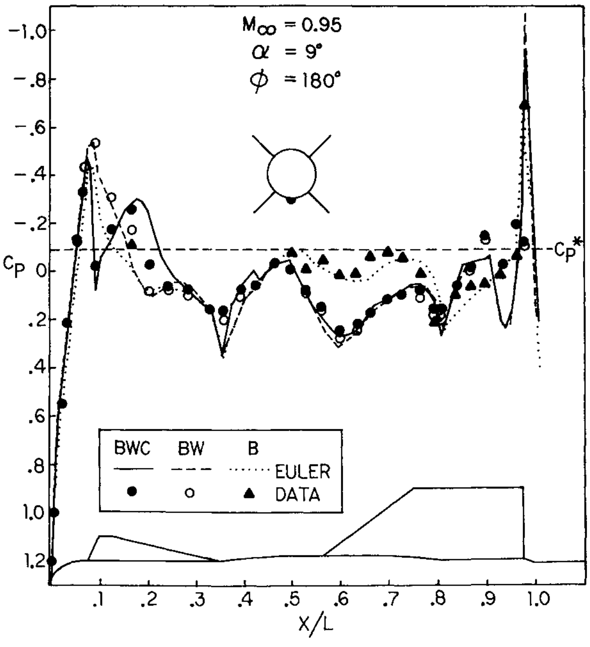

Fig. 8 Configurational effects, body windside.

Comparing the body-wing and body-alone curves, a significant difference is observed. In addition to the obvious effect at the wing section itself, the wings affect the flow upstream. The re-expansion after the nose-body shock is reduced at $X/L = 0.2$ as well as the expansion at the midbody at $X/L = 0.48$. On the windward side of the body, Fig. 8, the effect of the wings is not as evident, except, of course, at the wing section itself. Instead, the significant difference is due to the canard. The canard sets up a double-shock phenomenon: one shock at $X/L = 0.09$, the other at $X/L = 0.22$. Both the body-wing and body-alone cases indicate only one shock ranging from $X/L = 0.13$ to 0.16. The canard, however, has little effect at the wing section location downstream.

To investigate the effects of the wings and canards on the body surfaces on either side, comparisons are made on both the upper and lower sets of fins at Mach 1.05 again at $\alpha = 9$ deg. Figure 9 compares body pressure distributions astride the upper wing and canard. The predictions at $\phi = 30$ deg (or 15 deg off the leeside of the wing and canard surfaces) show strong expansions at the canard and wing sections. At this higher Mach number, the flow does not become subsonic until at the end of the canard at $X/L = 0.32$. At the wing section, the flow begins to compress at $X/L = 0.8$ but remains supersonic before shocking down at $X/L = 0.92$. Interestingly, on the windward side, $\phi = 60$ deg, the shocks near the canard and wing trailing edges ($X/L = 0.32$, 0.92) are at the same locations as on the leeward side, $\phi = 30$ deg. However, two additional features are evident. First is the now-familiar expansion, compression, re-expansion, and re-compression phenomena in the canard area. This M-type behavior of the pressure distribution also was evident in Figs. 7 and 8. At the wing section, the windward side flow has less momentum than on the leeside and shocks down at $X/L = 0.8$, where the leeside compressed only slightly. The comparison with wind-tunnel data is very good over most of the body surface.

Around the lower wing and canard, Fig. 10, both curves are on the windward side of the body, although the curve at $\phi = 120$ deg is on the leeside of the wing and canard. Being on the leeside of the fin surfaces allows pressure expansion at the canard, $X/L = 0.12$, and at the wing, $X/L = 0.77$. The windward side, $\phi = 150$ deg, does not exhibit these strong expansions, although the expansion and compressions that do occur are at the same X/L locations. Again, the M-type phenomenon occurs in the canard region, resulting in a double shock on the $\phi = 150$ deg curve.

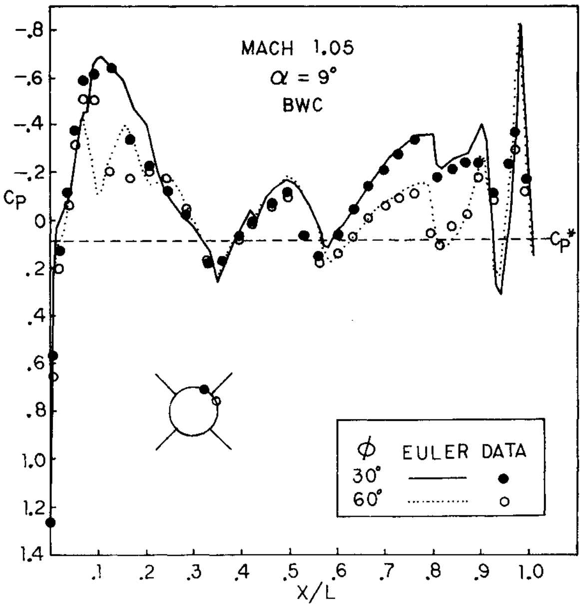

Fig. 9 Upper wing-canard effects on body.

To determine the effect the canards have on the wing surfaces themselves, pressure distributions on the body-wing and body-wing-canard configurations are examined. Figure 11 illustrates the effect of the canards on the upper wing at 42% span. The canard downwash effect lowers the angle of attack on the wings, as evident in the lower leading-edge expansion peak, $X/W = 0.22$, and midchord expansion at $X/W = 0.60$. The result is that the shock on the wing near $X/W = 0.70$ has moved upstream due to the canard. On the lower wing, Fig. 12, the canards seem to have little effect. What trend does exist is the same as in Fig. 11. The lack of interplay between the lower canards and wings indicates that little downwash effect exists for these sets of surfaces.

Mach Number Effects

To investigate the effect of Mach number on the configuration, a series of comparisons is made of the local surface Mach number on the body, wing, and canard. The local surface Mach number is plotted to allow easier comparison of subsonic and supersonic areas on specific locations on the configuration. A pressure coefficient plot would require multiple sonic pressure coefficient lines, making comparisons

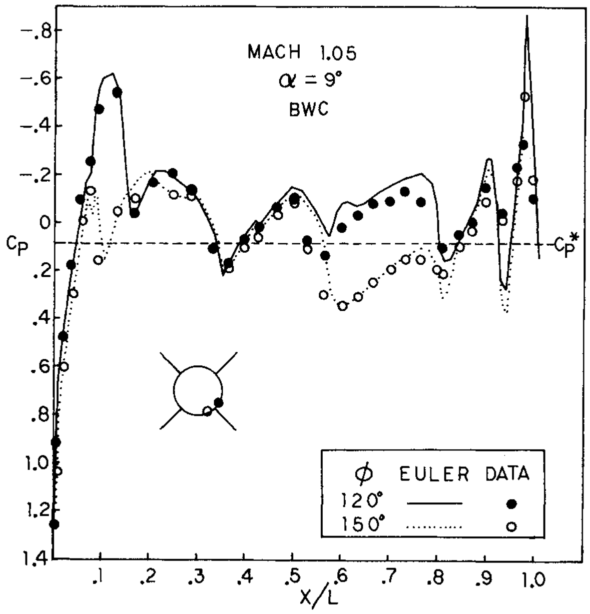

Fig. 10 Lower wing-canard effects on body.

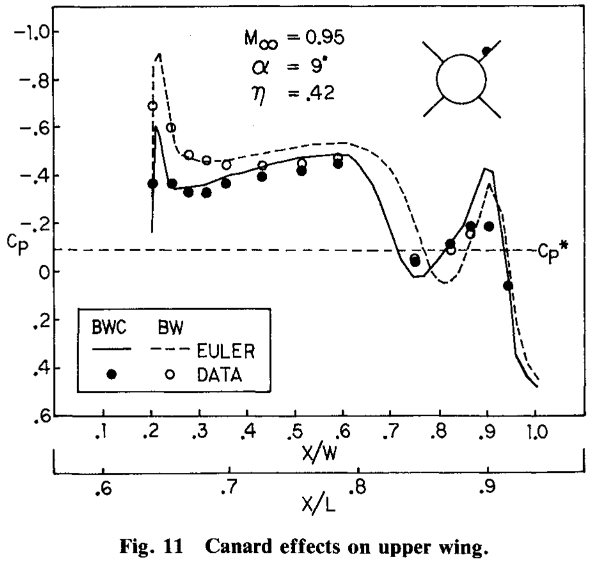

Fig. 11 Canard effects on upper wing.

more difficult. The local surface Mach number is obtained by applying the isentropic relationship between the pressure coefficient and Mach number. This is, of course, inexact, but since no velocity wind-tunnel data are available, it is the only means to put both computational results and wind-tunnel data on the same basis and to compare multiple freestream Mach numbers on the same plot. This procedure was applied to both the predicted and measured pressure results. An independent study comparing the local Mach obtained isentropically from predicted pressures with that calculated in the Euler code itself found that only a maximum of 4% difference was observed. Since this difference would be apparent in the computations as well as the data, it is concluded that relative positioning of the following curves and data remain the same whether isentropic or nonisentropic flow is assumed.

The effect of Mach number is first explored on the body surface. Figure 13 illustrates the differences in local Mach on the leeward side of the body. It is interesting to note that the double expansion peaks in the canard region are very similar in magnitude for Mach 0.95 and 1.05, yet the Mach 0.95 case shocks down much more rapidly. As expected, the expansions at the midbody and wing section are stronger for Mach 1.05. However, the wing remains supersonic for Mach 1.05, whereas it shocks at $X/L \doteq 0.8$ for Mach 0.95.

On the windward side, Fig. 14, the two curves display a similar and expected pattern downstream of the canard. In the nose-canard region, the initial expansion peaks are, again, nearly identical, yet the flow shocks much sooner for Mach 0.95. The additional energy in the Mach 1.05 flow delays the shock until the canard trailing edge, $X/L = 0.34$.

The effects of Mach number on the upper canard are shown in Fig. 15 at 30% span. Although the leading-edge expansions are strong, little difference is seen between Mach 0.95 and 1.05; however, the Mach 1.05 case remains supersonic whereas the Mach 0.95 case shocks down at $X/C = 0.45$. This pattern was seen on the body in Fig. 13. On the lower canard at 60% span, Fig. 16, the Mach effects are even less pronounced. Here both cases remain supersonic and the differences between the curves are expected.

The Mach number has a similar effect on both the wings and the canards. The upper wing, Fig. 17, shows a similar leading-edge expansion peak with the Mach 1.05 case remaining supersonic whereas the Mach 0.95 case shocks down at $X/W = 0.7$. The lower fin, Fig. 18, shows less Mach effect, as did the lower canard. Again, the comparisons of the computations with the data are very good for all cases presented.

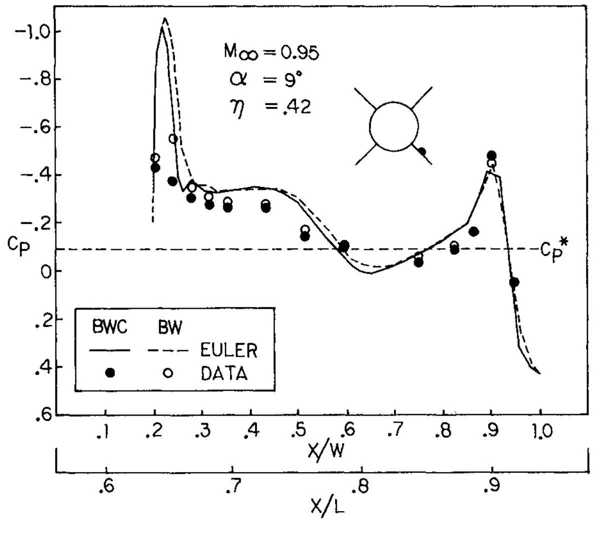

Fig. 12 Canard effects on lower wing.

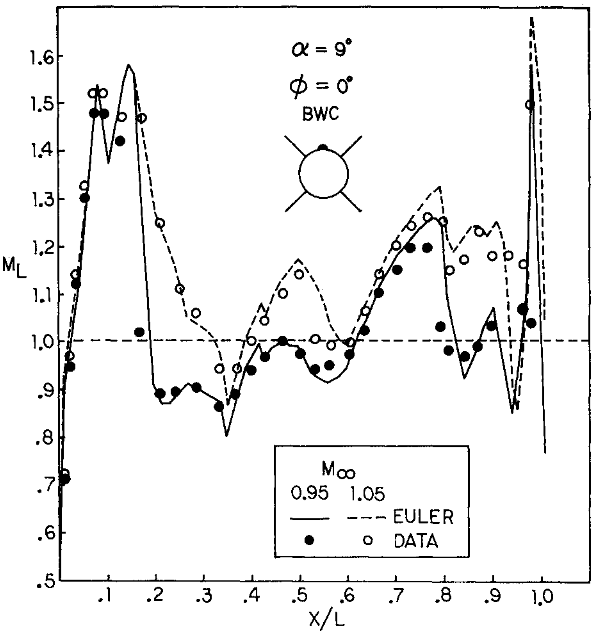

Fig. 13 Mach effects, body leeside.

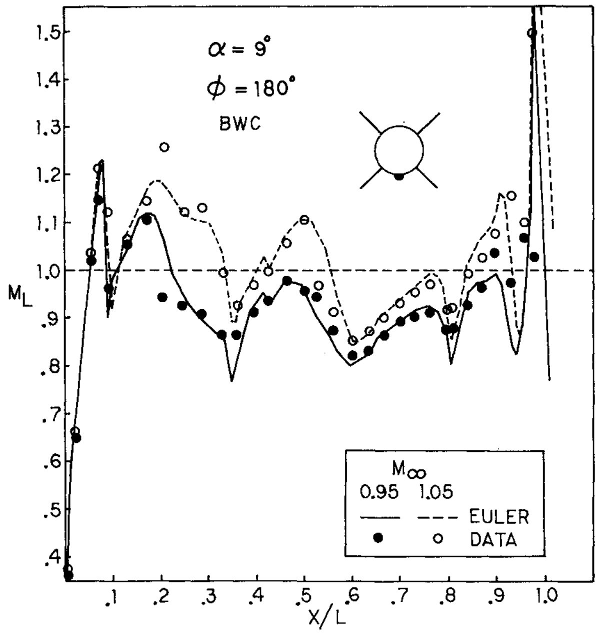

Fig. 14 Mach effects, body windside.

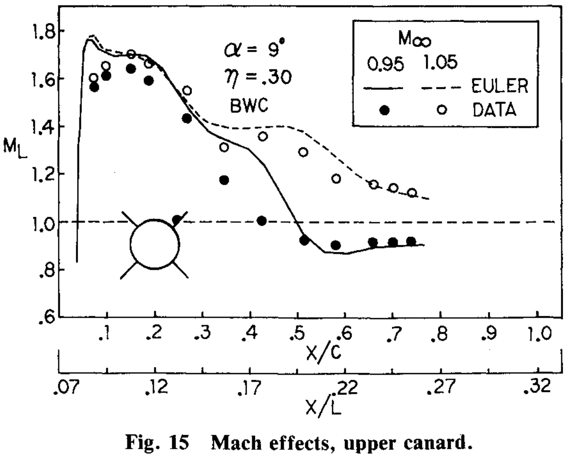

Fig. 15 Mach effects, upper canard.

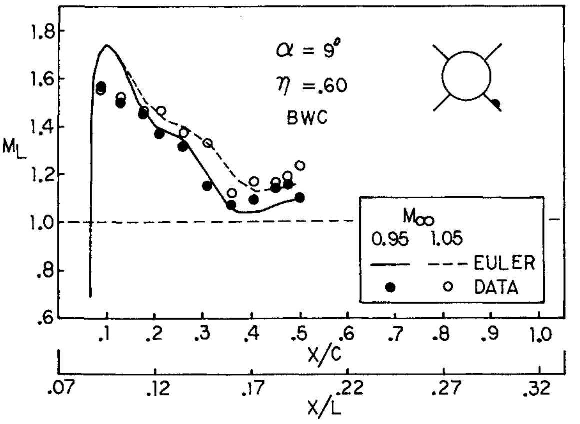

Fig. 16 Mach effects, lower canard.

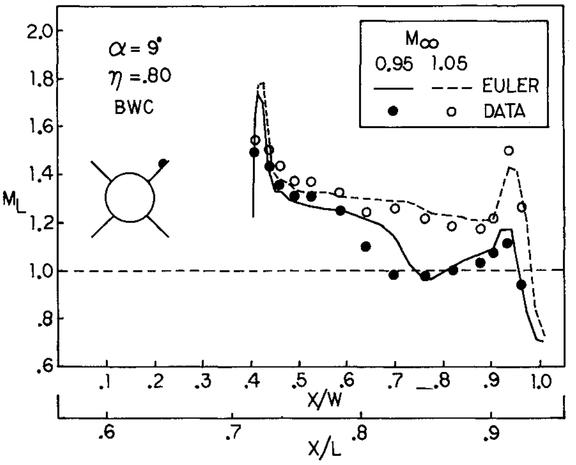

Fig. 17 Mach effects, upper wing.

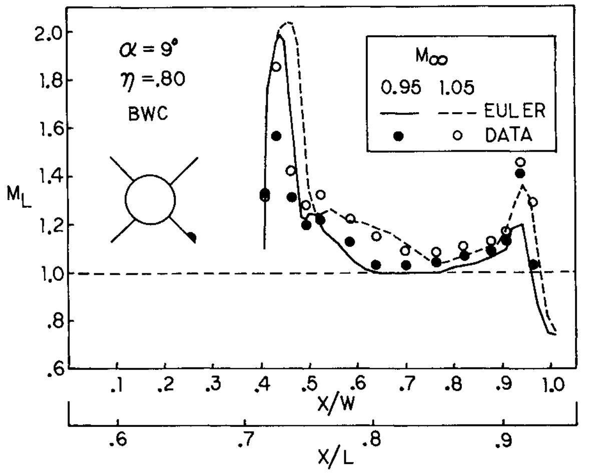

Fig. 18 Mach effects, lower wing.

Force and Center of Pressure

The pressure distributions calculated with the flow solver were integrated over the entire body-wing-canard configuration and compared to normal-force and center-of-pressure location results obtained from wind-tunnel data. Figure 19 plots normal force and center of pressure against angle of attack. Data were obtained only up to 10-deg angle of attack, whereas the predictions were carried out to 12 deg. The normal-force agreement is within 5%, even at angle of attack.

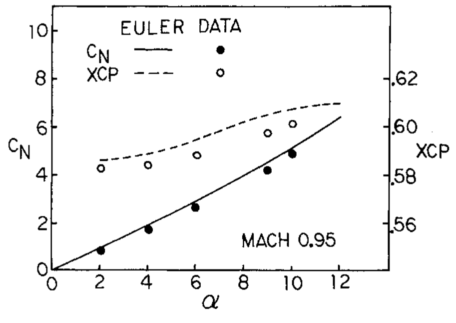

Fig. 19 Force and center-of-pressure results, varying angle of attack.

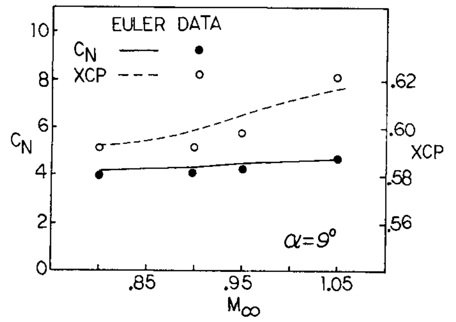

Fig. 20 Force and center-of-pressure results, varying Mach number.

The overprediction of normal force at angle of attack can be attributed to the inviscid nature of the flow solver. The Euler solver overpredicts the expansions on the leeside of the configuration while predicting the windward sides more accurately. This results in an overall prediction of lower pressure on the leeside of the configuration as compared to the wind-tunnel results and a net higher normal force in the leeside direction. Accounting for the viscous effects would result in better leeside expansion predictions and, consequently, a more accurate normal force. Discrepancy in the center of pressure location can be attributed to the same factor. The overpredicted normal force on the fins results in a more rearward center-of-pressure location than expected. Both the canards and wings contribute to the normal-force overprediction but yield opposite contributions to the center-of-pressure location. Since the wing surface area is approximately seven times that of the canard, the normal force contribution from the wings dominates the result in a more rearward location of the center of pressure. Nevertheless, the predicted center-of-pressure locations agree well with wind-tunnel-generated results, being within 1% of body length. This is important to the airframe designer because the accuracy of the center-of-pressure location reflects the accuracy of the force distribution. The normal-force and center-of-pressure results also were plotted against freestream Mach number, Fig. 20. The quality of the agreement between the predictions and data is similar to that in Fig. 19. Here, at a fixed angle of attack, the normal force is nearly constant from Mach 0.80 to 1.05. However, the data show that the center-of-pressure location moves rearward as expected in supersonic flow. The 2% rearward movement based on body length translates into a 5% rearward movement based on wing root chord. Although the Euler code does a good job predicting the magnitude of the total force, the predicted center of pressure moves rearward only 1% from Mach 0.95 to 1.05.

Conclusions

The split-flux-vector Euler solver is able to calculate exceptionally good engineering solutions on a blunt body of revolution with wings and canards at low-to-moderate angles of attack. The correlation between data and prediction is significant, considering the diversity of the configuration geometry that results in multiple shock patterns on the body, wings, and canards. In addition, this is the first successful near-sonic computational predictions on a blunt, low-aspect-ratio wing-canard configuration and the first step in the validation of the Euler code.

The effects of the wings and canards on the configuration were examined. The wings had an expected large effect on the configuration. The canards also had a significant effect in reducing the expansion strengths on the body and wings by creating a marked downwash effect. In the canard region itself, an M-type phenomenon occurred. This double expansion/compression occurrence is an important factor to a control system designer. The result is that the method presented here is a basic airframe design tool capable of providing engineering-design-quality aerodynamic characteristics.

References

[1] Boppe, C. W. and Stern, M. A., "Simulated Transonic Flows for Aircraft with Nacelles, Pylons, and Winglets," AIAA Paper 80-0130, Jan. 1980.

[2] Caughey, C. A. and Jameson, A., "Progress in Finite Volume Calculations for Wing-Fuselage Combinations," *AIAA Journal,* Vol. 18, Nov. 1980, pp. 1281-1288.

[3] Thomas, S. D. and Holst, T. L., "Numerical Computation of Transonic Flow About Wing-Fuselage Configurations on a Vector Computer," AIAA Paper 83-0499, Jan. 1983.

[4] Schmidt, W., Jameson, A., and Whitfield, D. L., "Finite Volume Solution for the Euler Equations for Transonic Flow Over Airfoils and Wings Including Viscous Effects," AIAA Paper 81-1265, June 1981.

[5] Weatherill, N. P. and Forsey, C. R., "Grid Generation and Flow Calculations for Complex Aircraft Geometries Using a Multi-Block Scheme," AIAA Paper 84-1665, June 1984.

[6] Shang, J. S., "Numerical Simulation of Wing-Fuselage Aerodynamic Interaction," AIAA Paper 83-0225, Jan. 1983.

[7] Thompson, D. S., "A Mesh Embedded Approach for Prediction of Transonic Wing-Body-Store Flowfields," Numerical Boundary Condition Procedures Symposium, Moffett Field, CA, 1981.

[8] Lijewski, L. E., "Transonic Flow Solutions on a Blunt, Finned Body of Revolution Using the Euler Equations," AIAA Paper 86-1082, May 1986.

[9] Thompson, J. F. and Warsi, Z. U. A., "Three-Dimensional Grid Generation from Elliptic Systems," AIAA Paper 83-1905, July 1983.

[10] Thompson, J. F., "A Composite Grid Generation Code for General Three-Dimensional Regions," AIAA Paper 87-0275, Jan. 1987.

[11] Martinez, A., Chae, Y.-S., and Thompson, J. F., "Applications of Numerical Grid Generation to Advanced Weapon Airframe Configurations," AIAA Paper 87-2294, Aug. 1987.

[12] Whitfield, D. L. and Janus, J. M., "Three-Dimensional Unsteady Euler Equations Solution Using Flux Vector Splitting," AIAA Paper 84-1552, June 1984.

[13] Warming, R. F. and Beam, R. M., "Upwind Second-Order Difference Schemes and Applications in Aerodynamic Flows," *AIAA Journal,* Vol. 14, Sept. 1976, pp. 1241-1249.